arXiv:1405.4133v1 [hep-ex] 16 May 2014

The first search for sub-eV scalar fields via four-wave mixing at a quasi-parallel laser collider

Kensuke Homma,[1,2] Takashi Hasebe,[1] and Kazuki Kume[1]

[1]*Graduate School of Science, Hiroshima University, Kagamiyama, Higashi-Hiroshima 739-8526, Japan*

[2]*International Center for Zetta-Exawatt Science and Technology, Ecole Polytechnique, Route de Saclay, Palaiseau, F-91128, France*

(Dated: May 19, 2014)

Abstract

A search for sub-eV scalar fields coupling to two photons has been performed via four-wave mixing at a quasi-parallel laser collider for the first time. The experiment demonstrates the novel approach to search for resonantly produced sub-eV scalar fields by combining two-color laser fields in the vacuum. The aim of this paper is to provide the concrete experimental setup and the analysis method based on specific combinations of polarization states between incoming and outgoing photons, which is extendable to higher intensity laser systems operated at high repetition rates. No significant signal of four-wave mixing was observed by combining a 0.2μJ/0.75ns pulse laser and a 2mW CW laser on the same optical axis. Based on the prescription developed for this particular experimental approach, we obtained the upper limit at a confidence level of 95% on the coupling-mass relation.

I. INTRODUCTION

A large fraction of dark components in the universe motivates us to search for yet undiscovered fields to naturally interpret the relevant observations. In high energy scales, several bosons have been discovered, which can be understood as a result of spontaneous symmetry breaking such as pions based on chiral symmetry at the 0.1GeV scale and W/Z bosons based on gauge symmetry via the Higgs mechanism at the 100GeV scale. The relevant experimental results show the evidence of coupling to two-photons of boson states, for instance, via the decay process of the neutral pion and the Higgs-like particle. These facts encourage further experimental searches for similar type of fields via two-photon coupling in very different energy scales even apart from any theoretical speculations. In addition, there are actually theoretical rationales to expect sub-eV particles such as the axion (pseudoscalar boson) [1] and the dilaton (scalar boson) [2] associated with breaking of fundamental symmetries in the context of particle physics and cosmology. Therefore, we are led to probe such fields via their coupling to two-photons in the sub-eV mass range. Furthermore, the advent of high-intensity laser systems and the rapid leap of the intensity encourage the approach to probe weakly coupling dark fields with optical photons by the enhanced luminosity factor [3, 4].

We advocated the concept of the quasi-parallel laser collider to produce a resonance state of a hypothetical boson in the sub-eV mass range and simultaneously induce the decay in the background of a coherent laser field [5–7]. The exchange of such a low-mass field is interpreted as the four-wave mixing process in the vacuum. Figure 1 illustrates the four-wave mixing process where two photons with the degenerate energy ω are used for the resonance production and the inducing laser field has the energy $u\omega$ with $0 < u < 1$, and a photon with the energy $(2-u)\omega$ is created as the signature of the interaction. This four-wave mixing process is well-known in quantum optics [8, 9], where atomic dynamics governs the phenomenon instead of the exchange of the hypothetical resonance state, and the application to test the higher-order QED effect can also be found in Ref. [10]. We identify this wave mixing system as a special kind of photon-photon colliders intentionally, whose significant advantage is that the interaction rate has cubic dependence on the laser intensity, while the conventional particle colliders have quadratic dependence on the number of charged particles per colliding bunch [7]. The cubic dependence of the interaction rate highly motivates us to extend the method to much higher pulse energy and higher-intensity laser systems.

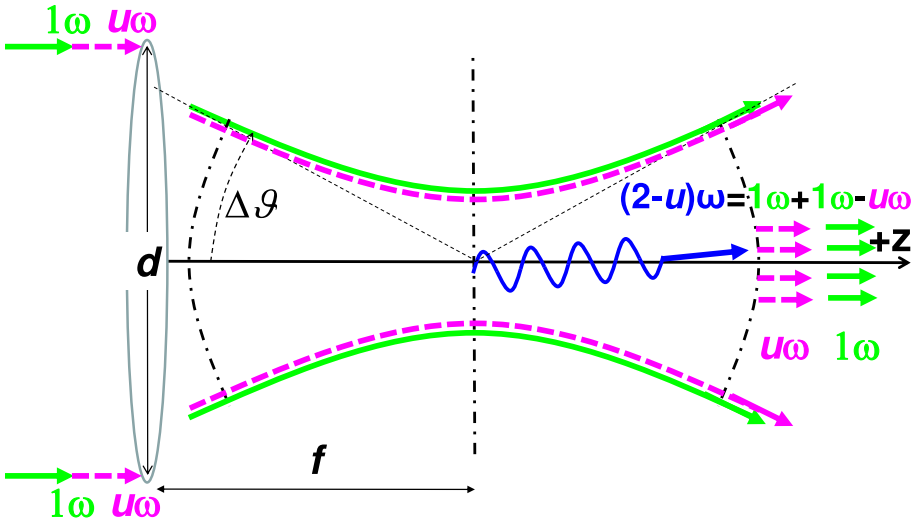

FIG. 1: Quasi parallel colliding system (QPS) between two incident photons out of a focused laser beam with the focal length f, the beam diameter d, and the upper range of incident angles $\Delta\vartheta$ determined by geometric optics. The signature $(2-u)\omega$ is produced via the four-wave mixing process, $1\omega + 1\omega \rightarrow (2-u)\omega + u\omega$ with $0 < u < 1$ by mixing two-color waves with different frequencies 1ω and $u\omega$ in advance at the incidence.

The proposed method can in principle distinguish whether the exchanged boson is scalar or pseudoscalar based on combinations of polarization states in the initial and final state photons [7]. Therefore, the method has impacts on searches for axion-like particles as well as the fifth force[11]. In this paper, however, we focus only on the case for the scalar field exchange, because the experimental setup is simpler. The aim of this paper is to demonstrate the pilot experiment to search for sub-eV scalar fields via the four-wave mixing process in the vacuum, in which basic elements necessary for the proposed experimental method and the data analysis are provided so that they can be extended to much higher-intensity systems operated at high repetition rates in the near future [12].

II. COUPLING-MASS RELATION

In this section we summarize formulae necessary to obtain the coupling-mass relation from experimental parameters. The formulae are basically from Ref. [7], however, we re-evaluate the relations to apply to the realistic experimental conditions in the pilot search. We thus provide the details of the corrections in Appendix A and B compared with those in Ref.[5, 7].

The effective interaction Lagrangian between two photons and a hypothetical low-mass scalar field has the generic form expressed as

$$-L_\phi = gM^{-1}\frac{1}{4}F_{\mu\nu}F^{\mu\nu}\phi \tag{1}$$

where M has the dimension of energy while g being a dimensionless constant.

In the case of the scalar field exchange, the possible linear polarization states in the four-wave mixing process when all wave vectors are on the same plane as illustrated in Fig.2 are expressed as follows:

$$\begin{aligned}\omega\{1\}+\omega\{1\} &\rightarrow (2-u)\omega\{1\}+u\omega\{1\} \\ \omega\{1\}+\omega\{1\} &\rightarrow (2-u)\omega\{2\}+u\omega\{2\},\end{aligned} \tag{2}$$

where photon energies from the initial to the final state are denoted by the linear polarization states $\{1\}$ and $\{2\}$ which are orthogonal to each other. In this pilot experiment, we pursuit the second case of Eq.(2).

We then introduce notations to describe kinematics of four photons as illustrated in Fig.2, where the incident angle ϑ is assumed to be symmetric around the z-axis in the average sense, because we focus lasers symmetrically by a lens element. We introduce an arbitrary number u with $0 < u < 1$ to re-define momenta of the final state photons as

$$\omega_4 \equiv u\omega \quad \text{and} \quad \omega_3 \equiv (2-u)\omega, \tag{3}$$

where we require $0 < \omega_4 < \omega_3 < 2\omega$. We consider to measure ω_3 with the specific polarization states as the signature of the interaction. With these definitions, energy-momentum conservation is expressed as [7]

$$(2-u)\omega + u\omega = 2\omega, \tag{4}$$

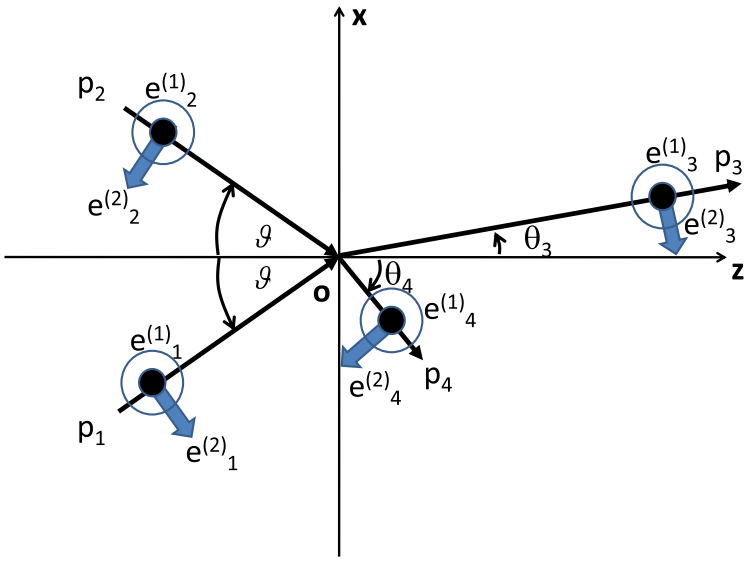

FIG. 2: Definitions of kinematic variables [5].

$$(2-u)\omega\cos\theta_3 + u\omega\cos\theta_4 = 2\omega\cos\vartheta, \tag{5}$$

$$(2-u)\omega\sin\theta_3 = u\omega\sin\theta_4, \tag{6}$$

$$\mathcal{R} \equiv \frac{\sin\theta_3}{\sin\theta_4} = \frac{\omega_4}{\omega_3} = \frac{u}{2-u} = \frac{\sin^2\vartheta}{1-2\cos\vartheta\cos\theta_4+\cos^2\vartheta}. \tag{7}$$

Given a set of physical parameters of the scalar field exchange: mass m, coupling to two photons g/M, and the polarization dependent factor $\mathcal{F}_S$ with a specified set of linear polarizations S as explained below, the yield is parameterized as

$$\mathcal{Y} \equiv \frac{1}{64\sqrt{2}\pi^4}\left(\frac{\lambda_c}{c\tau_c}\right)\left(\frac{\tau_c}{\tau_i}\right)\left(\frac{f}{d}\right)^3 \tan^{-1}\left(\frac{\pi d^2}{4\ f\lambda_c}\right)\frac{(\overline{u}-\underline{u})^2}{\overline{u}\underline{u}}\left(\frac{gm[eV]}{M[eV]}\right)^2\left(\frac{m[eV]}{\omega[eV]}\right)^3 \mathcal{W}\mathcal{F}_S C_{mb} N_c^2 N_i, \tag{8}$$

which is quoted from Eq.(57) in Appendix A, where the subscripts c and i denote creation and inducing lasers, respectively, λ wavelength, τ pulse duration, f a common focal length, d a common beam diameter, $\overline{u}$ and $\underline{u}$ upper and lower values on u determined by the spectrum width of ω_4, respectively, $C_{mb} = 1/2$ is the combinatorial factor originating from the consideration on multimode frequency states [7], N the average numbers of photons in coherent states, $\mathcal{W} \sim \pi/2$ the numerical factor relevant to the integral of the weighted resonance function defined by Eq.(44) in Appendix A, and we partially apply natural units to parameters specified with [eV].

We have discussed the effect of the spectrum width in the case that the spectrum width of the creation laser is negligibly small compared to that of the inducing laser in Ref.[7]. However, this is not always the case. For example, this pilot experiment is actually performed with the condition that both widths are nearly equal as we explain in the next section. We provide the treatment on the effective choice of $\overline{u}$ and $\underline{u}$ applicable to the most general case in Appendix B in detail.

In the case of $S = 1122$ as specified by the second of Eq.(2) applied to the scalar field exchange (SC), the polarization dependent factor is estimated as [7]

$$\mathcal{F}^{SC}_{1122} \sim 2\pi \left(\frac{3}{8} + 3\hat{\mathcal{R}}^2 - \hat{\mathcal{R}} \right) \tag{9}$$

with $\hat{\mathcal{R}} \equiv \frac{1}{2}(\mathcal{R} + \mathcal{R}^{-1})$ for a given u via $\mathcal{R}$ in Eq.(7). This factor originates from a degree of freedom on the azimuthal rotation of the plane including p_3 and p_4 around the z-axis in Fig.2 with respect to that defined by p_1 and p_2. The other polarization combinations can also be calculated based on Appendix of Ref.[7].

From Eq.(8) we express the coupling parameter g/M to discuss the sensitivity as a function of m for a given set of experimental parameters via the following equation

$$\frac{g}{M[eV]} = 2^{1/4} 8\pi^2 \sqrt{\frac{\mathcal{Y}\omega^3[eV]}{\left(\frac{\lambda_c}{c\tau_c}\right)\left(\frac{\tau_c}{\tau_i}\right)\left(\frac{f}{d}\right)^3 \tan^{-1}\left(\frac{\pi d^2}{4\ f\lambda_c}\right) \frac{(\overline{u}-\underline{u})^2}{\overline{u}\,\underline{u}} \mathcal{W}\mathcal{F}_S C_{mb} N_c^2 N_i}} m^{-5/2}[eV] \tag{10}$$

under the condition $\tau_c \leq \tau_i$, because the pulse energy of the creation laser is more important to enhance the signal yield due to the quadratic dependence on the energy.

III. EXPERIMENTAL SETUP TO DETECT FOUR-WAVE MIXING

Figure 3 shows the schematic view of the experimental setup. The setup consists of the wave mixing part (WM), the interaction vacuum chamber (IC), the intensity monitoring part (IM) and the single photon detection part (SPD).

WM combines a pulsed laser beam to create a resonance state with a continuous wave (CW) laser beam which induces the decay with specified linear polarization states. For the purpose of the calibration, a laser beam containing the signal energy $(2-u)\omega$ is also combined. The wave mixing can be achieved by a set of dichroic mirrors.

The pulsed laser is the linearly polarized NanoLaser, a monolithic passively Q-switched microchip laser . The laser cavity consists of a 2mm^3 Nd:YAG gain medium bonded to

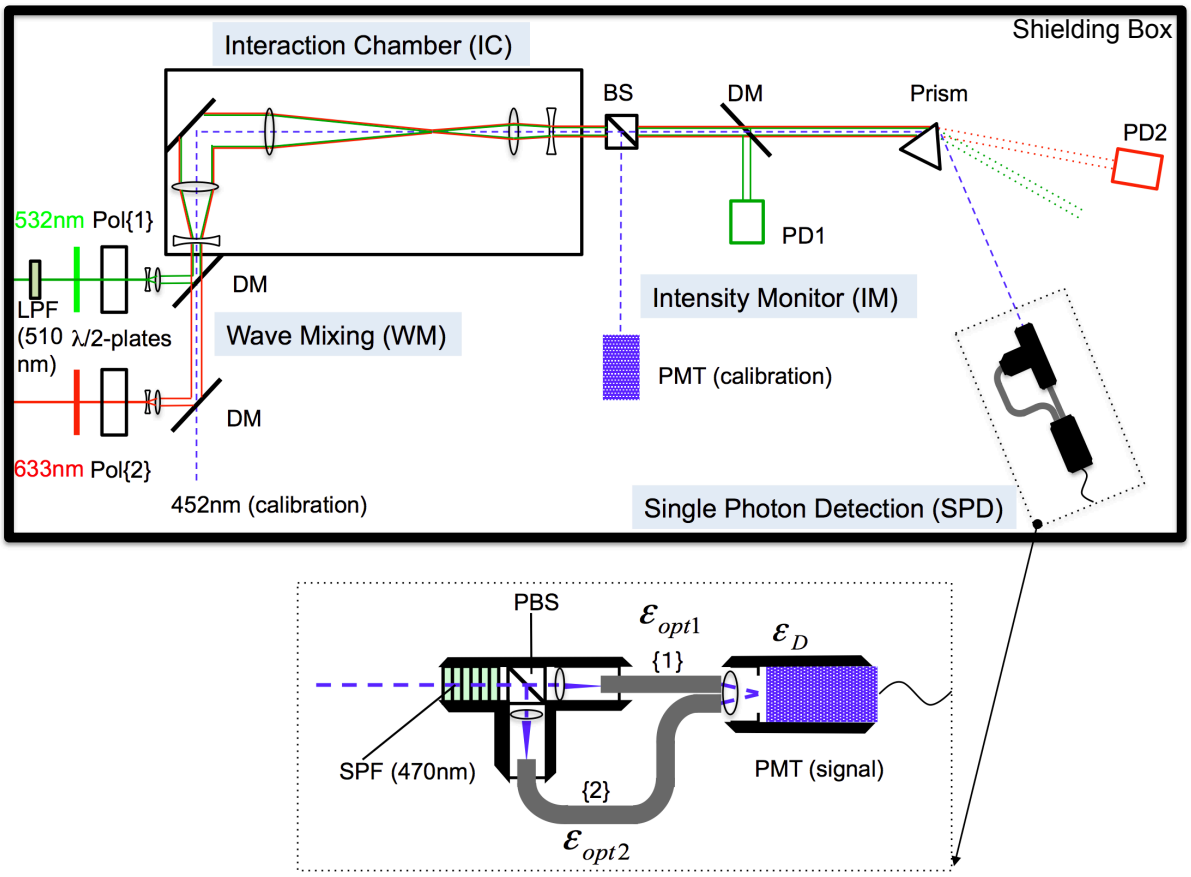

FIG. 3: Schematic view of the experimental setup to measure the four-wave mixing process in the vacuum.

a chromium doped YAG saturable absorber. The repetition rate depends on the diode pumping power: the higher the pumping power, the faster the absorber saturates at which the absorber becomes transparent. The measured repetition rate is 18.5 kHz. The cavity's mirrors are vapor deposited on the both sides of the crystal to form a monolithic oscillator pumped by a CW diode laser. The second harmonic wavelength 532nm is produced by converting the fundamental wavelength 1064nm. The pulse energy of the 532nm wave is typically 0.8μJ per 0.75 ns pulse duration with the transverse mode close to TEM00 at the ejection point of the laser.

The CW laser is the linearly polarized Helium-Neon laser at the wavelength 632.8 nm with the power 10mW at the ejection point of the laser and the transverse mode TEM00.

Relative line widths of these lasers with respect to their central frequencies are summa-

rized in Tab.II, respectively. In addition, as we discuss in Appendix B about the relation on line widths between creation and inducing lasers which is relevant to $\overline{u}$ and $\underline{u}$ in Eq.(8), we evaluate the effective line width in the averaged quasi-parallel frame based on Eq.(83) in Appendix B.

Given wavelengths for creation laser ($\lambda_c = 532$ nm) and inducing laser ($\lambda_i = 633$ nm) beams which result in $u = \lambda_c/\lambda_i = 0.84$, the corresponding wavelength of four-wave mixing is expected to be

$$\lambda_s = \frac{\lambda_c/2 \cdot \lambda_i}{\lambda_i - \lambda_c/2} = 459 \text{ nm}. \tag{11}$$

Thus, in addition to the creation and inducing laser beams, a blue diode laser covering the 452 ± 10nm wavelength range is used to supply the calibration source to align the detection system and to obtain the detector efficiency with respect to the signal photon of $(2-u)\omega$.

The linear polarizers made of calcite with the extinction ratio of $O(10^{-4})$ specifies the incident linear polarization states of the creation and inducing laser fields as well as the calibration laser field, respectively. The linear polarization state $\{1\}$ is determined by the polarizer (Pol$\{1\}$) for the creation laser, while the state $\{2\}$ is set by the polarizer (Pol$\{2\}$) for the inducing laser which is adjusted so that the planes of the linear polarizations become orthogonal to each other. In front of the linear polarizers, $\lambda/2$-plates are placed and adjusted so that the transmittance of almost linearly polarized lasers at the output of the laser systems is maximized. In front of the ejection point of the creation pulse laser, we put a long pass filter to accept wavelength only above 510 nm to suppress wavelength close to the signal wavelength 459 nm in advance of the wave mixing with the optical density OD~ 4 where OD is defined as OD$\equiv -\log_{10}(I/I_0)$ with output and input photon intensities I and I_0, respectively.

After wave mixing with specified polarization states, the combined laser beams share the common optical axis, and they are guided into the interaction chamber (IC) maintained at 1.2×10^{-4}Pa. Inside IC, a set of achromatic lenses expands the beam diameter to 40 mm and focuses the combined beams with the focal length $f = 200$ mm. The focal spots are monitored by a beam profile monitor and the centers of the two-color beam profiles at a point near from the common focal spot are aligned to each other with $\sim 10\mu$m precision. The agreement of the optical axes between the two beams are also confirmed by checking the profile overlap at a different point from the focal spot along the common optical axis. After focusing the combined beams inside IC, the divergent beams are parallelized by a set of

achromatic lenses with the reduced beam diameter 10 mm and guided to outside IC through the chamber window. The beam focusing parameter is important, because this gives the upper limit of the sensitive mass range by the possible range of the incident angle ϑ via Eqs.(40) - (42) in Appendix A. The resonance production is enhanced when $m = 2\omega \sin\vartheta$ is satisfied, that is, when a CMS-energy between two incident photons coincides with the exchanged mass. If an angular coverage $\Delta\vartheta$ is too small compared to a mass we are interested in, the resonance condition is never satisfied. Therefore, the focusing parameter can adjust the sensitive mass range via the upper limit on the incident angles. In this pilot experiment the upper limit on mass is thus 0.46 eV for the creation laser wavelength of 532 nm (2.3 eV).

The absolute beam intensities are monitored by the beam profile monitor. The non-interacting creation and inducing laser fields are kicked out by individual dichroic mirrors and the reflected waves are measured by the photo diodes PD1 and PD2 for 532 nm and 633 nm, respectively. These amplitude information are used to monitor the relative intensity variation on the shot-by-shot basis.

The signal wave is further guided to the equilateral prism made of N-SF11 glass with the MgF_2 anti-reflection coat and refracted to the detection system, while the residual non-interacting creation and inducing beams are refracted to different directions. These non-interacting waves are further reflected by mirrors and dumped apart from the detection point of the signal wave.

For the scalar field search, we require the initial and final state photon energies with their linear polarization states as follows

$$\omega\{1\} + \omega\{1\} \to u\omega\{2\} + (2-u)\omega\{2\}, \tag{12}$$

where $\{1\}$ and $\{2\}$ specifies the orthogonal linear polarization states for photons in the creation beam and in the inducing beam, respectively. As a reference polarization combination, we also measure the following case simultaneously

$$\omega\{1\} + \omega\{1\} \to u\omega\{2\} + (2-u)\omega\{1\}, \tag{13}$$

which is not allowed when all wave vectors in Fig.2 are on the same plane. Due to a degree of freedom on the relative rotation angle between $p_1 - p_2$ and $p_3 - p_4$ planes around the z-axis, however, there is a finite probability to accept this polarization combination. In order to measure the both cases on the shot-by-shot basis, we introduced the polarization beam

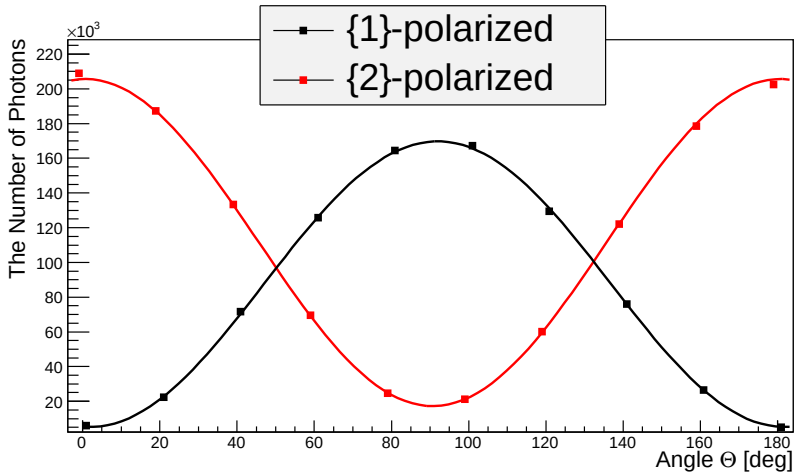

FIG. 4: The number of photons in $T\{1\}$ and $T\{2\}$ as a function of the relative rotation angle between the polarization plane of the pulsed creation laser and that of the polarization beam splitter (PBS).

splitter (PBS) whose polarization directions are aligned to the incident laser polarizations $\{1\}$ and $\{2\}$ in advance, respectively (see the enlarged view of the SPD part in Fig.3). For the two polarization paths behind the PBS, two plastic optical fibers whose transmittance are independent of the incident linear polarization states are attached with different lengths by introducing a relative time delay 23.75 ns. These two optical fibers are attached to a common photomultiplier tube (PMT), which is a metal package PMT with the rise time 0.78 ns (R7400-01 manufactured by HAMAMATSU), through lenses so that we can count the number of photons in the two different time domains $T\{1\}$ and $T\{2\}$ separated by that time difference on the digitized wave form of the analog output from the common PMT. By using the fiber-coupled PMT, the degree of the linear polarization is measured by rotating the polarization plane of the pulsed creation laser with respect to that of the PBS. Figure 4 shows how the number of photons in $T\{1\}$ and $T\{2\}$ change as a function of the relative rotation angle Θ in units of degree, respectively. The fit results with the functional form $\sin(\pi\Theta/180)$ are consistent with a nearly linear polarized state after transmission though all of optics including dichroic mirrors.

In order to shutout residual non-interacting creation and inducing laser photons, five short pass filters (SPF) with the nominal OD$\sim$ 4 for each to accept only wavelength below 470 nm are placed inside the tube in front of the PBS. The detection efficiency to the signal

wavelength is evaluated in advance of the pilot measurement with the two same-type PMT's with the beam splitter(BS) in Fig.3.

The readout of the analog signal from the photomultiplier is performed by 4-ch waveform digitizer (10-bit cPCI High-Speed Digitizers, Acqiris DC282 type U1065A provided by Agilent Technologies) without any electronics for amplification to avoid adding noise sources. The measured maximum rate of the readout by requiring simple online preselections is $\sim$ 10 kHz. The digitizer is similar to the digital oscilloscope, however, the readout speed is three orders of magnitude higher. Thus online selections based on an algorithm are applicable before waveforms are actually stored.

Trigger signals are created by discriminating pulse heights of analog signals on PD1 and the digitizer is synchronized with these trigger signals. By denoting the existence or absence of green (532 nm) and red (633nm) lasers as g and r or $\bar{g}$ and $\bar{r}$, respectively, we can consider following four wave-mixing patterns: $g+r$, $\bar{g}+\bar{r}$, $g+\bar{r}$, and $\bar{g}+r$ representing cases including signal (S), dark currents or pedestal (P), residual of creation laser photons (C), and residual of inducing laser photons (I), respectively. The pedestal trigger is produced immediately after every 18.5 kHz green triggers by adding a constant delay at which the green laser pulse is physically absent.

We put a physical shutter on the CW red laser beam line repeating open and close every 2 sec. Monitoring the green and red laser amplitudes at individual triggers allows to identify the four patterns of wave-mixing S, P, C and I based on the offline analysis on the recorded digitized waveform. Waveforms are recorded with 500 sampling points during the 250 ns time window corresponding to 0.5 ns/division which is consistent with the time resolution on the leading edge of the used photomultiplier(PMT) for the single photon detection.

As the online level trigger, we required that at least one signal-like signature below -1.00 mV threshold after online pedestal subtraction is found in either $T\{1\}$ or $T\{2\}$ time domain within the two 15 ns windows (see green bands in Fig.5 and 7), and only waveforms containing such a signature are recorded on the disk for the offline analysis.

The number of total triggers reached 2.5×10^9 during the pilot measurement over four days.

IV. OFFLINE DATA ANALYSIS

In order to test statistical significance of four-wave mixing signals, the quantities we discuss are N_{Si} which are acceptance-uncorrected numbers of photons found in the time domains $T\{i\}$ with the linear polarization states $i = 1, 2$ in the case of the signal pattern (S). For the following paragraphs, we abbreviate the symbols of the time domains with specified polarization states, unless confusion is expected.

First, the four patterns: signal (S), pedestal (P), residual of green laser photons (C) and residual of red laser photons (I) are identified by looking at amplitudes of photodiodes recorded in the waveform data, and the number of events of individual patterns: W_S, W_P, W_C and W_I, respectively, are counted. These numbers are used as the weights to evaluate the number of photons in the signal pattern by subtracting those in the other patterns.

Since there is no complete wave filters, we must expect non-zero numbers of residual photons in the three patterns except the pedestal pattern where the dominant background is the thermal noise from the photomultiplier. We, therefore, interpret the observed raw numbers of photons n in the four patterns specified with individual subscripts as

$$\begin{aligned} n_S &= N_P + N_C + N_I + N_S \\ n_C &= N_P + N_C \\ n_I &= N_P + N_I \\ n_P &= N_P, \end{aligned} \tag{14}$$

where we assume that the observed pedestal counts include thermal noises from the photodevice and ambient noises such as cosmic rays, hence, the pedestal counts should be commonly included in the other three patterns in the average sense. By considering the event weights of the four trigger patterns, we then deduce the true number of photons in the signal pattern as follows

$$\begin{aligned} N_S &= n_S - \frac{W_S}{W_P} n_P - \frac{W_S}{W_C}(n_C - n_P) - \frac{W_S}{W_I}(n_I - n_P) \\ &= n_S - \frac{W_S}{W_C} n_C - \frac{W_S}{W_I} n_I + \frac{W_S}{W_P} n_P. \end{aligned} \tag{15}$$

We note that, exactly speaking, the physical meaning of n_P is different from the number of photons, because the dominant pedestal charges are produced by thermal noises of the

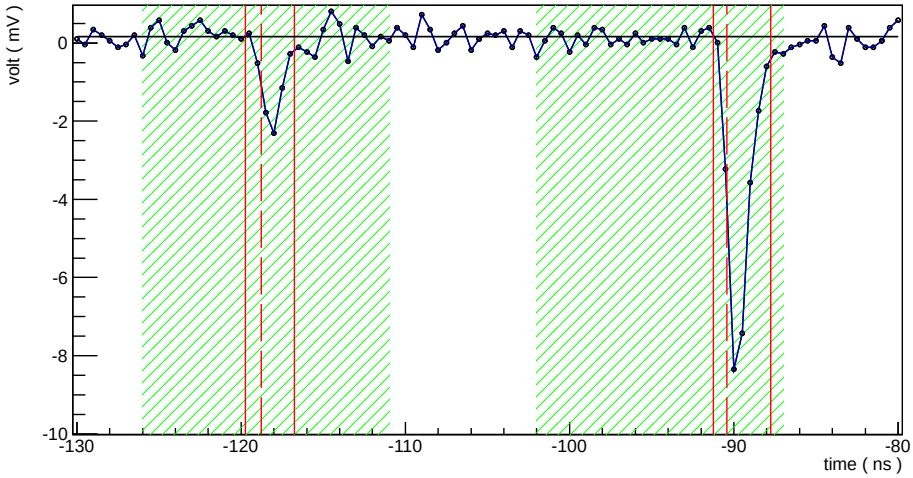

FIG. 5: Single shot example of a digitized waveform with peaks within the 50 ns time window.

photodevice. As long as observed charges are expressed in units of single-photon equivalent charge, however, this treatment is justified.

The analysis steps to obtain observed raw numbers n_{ij} with trigger patterns $i = S, C, I, P$ and linear polarization states $j = 1, 2$ are as follows. Figure 5 shows a single shot example of the digitized waveform within a 50 ns time window. The two time domains within a 3.5 ns interval subtended by two solid vertical lines, respectively, are equally defined which are separated by the known time difference of 23.75 ns due to the different optical fiber lengths. The shorter (earlier time domain) and longer (later time domain) fibers correspond to the linear polarization states $\{1\}$ and $\{2\}$, respectively.

Photon-like signals or thermal noise signals are identified by the negative peak finding. After finding a time bin with the largest amplitude in the negative direction, a global pedestal amplitude is determined by averaging over the 250 ns window excluding the peak region as shown by the horizontal line in Fig.5. We then find the falling edge and define the signal arrival time t_0 at the detector as the time bin at the half value of the peak amplitude after subtracting the pedestal value, which is indicated by the dotted vertical line. We require that a peak structure is identified by a pair of falling and rising edges around the peak position t_p. By defining time intervals from the falling edge to the peak and the peak to the rising edge as Δt_f and Δt_r, respectively, the time window of a signal, t_{sig}, is defined as $t_p - 2.0\Delta t_f \leq t_{sig} \leq t_p + 2.25\Delta t_r$ which are indicated by solid vertical lines. The charge sum

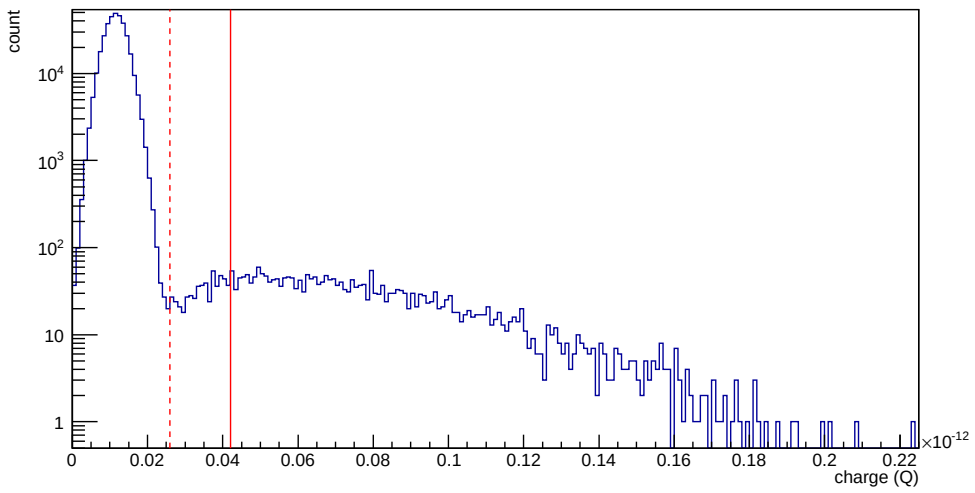

FIG. 6: Charge sums within time windows of photon-like signals in the all four trigger patterns. The offline cut is indicated by the dotted vertical line with respect to the solid vertical line corresponding to single-photon equivalent charge.

in that time window is evaluated in units of single-photon equivalent charge -4.21×10^{-14} C.

The single-photon equivalent charge from the used PMT operated at -800 V was evaluated with weak pulsed photon sources ranging from 0 to several tens photons as the average number of incident photons per pulse injection. Based on the Poissonian probability distribution for a given set of the pulsed photon sources, we can estimate the expected charge when a single photon is injected so that this charge is common to all the weak photon sources.

We then choose the waveforms satisfying the condition that at least one peak above 0.6 photon equivalent charge ($-2.60 \times 10^{-14}/-4.21 \times 10^{-14}$) is contained for counting the number of photons in the four patterns. The offline cut is indicated by the dotted vertical line in Fig.6 with respect to single-photon equivalent charge denoting by the solid vertical line, where the charge sums within time windows of photon-like signals are shown in the all four trigger patterns.

Figure 7 shows charge sums within time windows of peak-like structures, equivalently the numbers of photon-like signals, as a function of the observed arrival time t_0 for the four trigger patterns. The number of photons is counted in units of single-photon equivalent charge within the time domains $T\{1\}$ and $T\{2\}$, respectively. Table I summarizes the

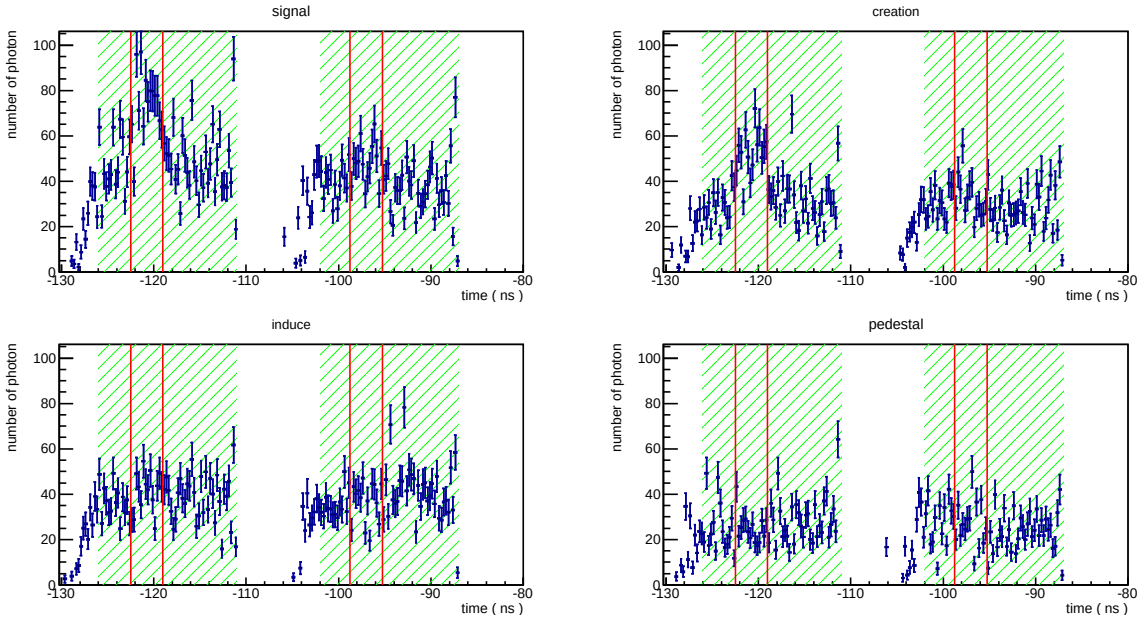

FIG. 7: Charge sums within time windows of peak-like structures in units of single-photon equivalent charge that correspond to the numbers of photon-like signals, as a function of the arrival time t_0 for the four trigger patterns : signal, pedestal, green residual and red residual within the time domains $T\{1\}$ and $T\{2\}$ with a 3.5 ns interval subtended by the red vertical lines, respectively. The green shaded bands indicate the online analysis windows of 15 ns time duration.

number photons in units of single-photon equivalent charge in the four trigger patterns in the time domains $T\{1\}$ and $T\{2\}$, respectively, with the number of analyzed events in trigger patterns $i = S, C, I, P$, respectively.

V. RESULTS

We take two steps to discuss the existence of signal photons from the four-wave mixing process. First, we investigate whether the acceptance-uncorrected N_{S1} and N_{S2} indicate deviations from zero beyond the inclusive errors in individual polarization paths. We then set upper limits on the coupling-mass relation, if there is no statistically significant number of four-wave mixing signals. Otherwise, we discuss the polarization dependence of the observed finite numbers of four-wave mixing signals.

The acceptance-uncorrected numbers of photon-like signals N_{S1} and N_{S2} with signal

Trigger i	n_{i1}	n_{i2}	W_i
S	1036	675	5.97317383×10^8
P	391	422	6.65181553×10^8
C	822	513	6.65200665×10^8
I	574	510	5.97300398×10^8

TABLE I: Observed raw numbers of photon-like signals n_{ij} in two time domains specified with the polarization states $j = 1, 2$ for each trigger pattern $i = S$(signal), P(pedestal dominated by thermal noise), C(green laser), and I(red laser) where W_i indicates the number of analyzed events in trigger pattern i.

triggers(S) after subtraction between four patterns of triggers were obtained based on the relation in Eq.(15) as follows:

$$N_{S1} = 75 \pm 51(stat.) \pm 96(syst.I) \pm 7(syst.II), \tag{16}$$
$$N_{S2} = 83 \pm 44(stat.) \pm 96(syst.I) \pm 7(syst.II).$$

The statistical errors were calculated by taking propagation of statistical errors associated with the subtraction using the photon numbers in Tab.I into account. The systematic errors I associated with the subtraction between four trigger patterns were evaluated by focusing on the behavior of the numbers of photon-like signals in the time windows outside $T\{1\}$ or $T\{2\}$ domains, denoting by $\overline{T\{1\}}\&\overline{T\{2\}}$, where only unpolarized background photon-like signals are expected [1], hence, the difference between $N_{S\overline{1}}$ and $N_{S\overline{2}}$ should not appear and the deviation from zero gives the systematic uncertainty on the subtraction method. We randomly combined 14 independent time bins of 0.25ns interval among the $\overline{T\{1\}}\&\overline{T\{2\}}$ domain and count the number of photon-like signals within the same time window as that of $T\{1\}, T\{2\}$ domains, *i.e.*, 3.5ns = 0.25ns $\times$ 14. The root-mean square of such counts even-

[1] The residual of pulsed creation laser beam is only found either in $T\{1\}$ or $T\{2\}$ domains, even though the polarization states can be distinguished by the two optical fiber paths. On the other hand, the residual of the CW inducing laser beam can be found in any time domains, however, the polarization states cannot be distinguished by the two optical fiber paths eventually, because photons even with one polarization state can produce signals in the two time domains equally as long as these incident timings are randomly distributed. Therefore, if $\overline{T\{1\}}\&\overline{T\{2\}}$ domain is chosen, no polarization dependence of the number of residual photon-like signals is expected after all, as long as the subtraction between four trigger patterns is ideally performed. Needless to say, thermal noises should not have the polarization dependence.

tually gives the systematic uncertainty on the baseline counts in $T\{1\}$ and $T\{2\}$ domains associated with the subtraction method. The systematic errors II originates from the ambiguity on the offline cut to define a peak to count the number of photon-like signals. These are estimated by changing the offline cut value from 0.5 to 2.0 photon equivalent charge. The numbers in Eq.(16) indicate there is no significant four-wave mixing signal within one standard deviation in the both polarization states $\{1\}$ and $\{2\}$ [2].

In order to evaluate the acceptance-corrected photon numbers $\mathcal{N}_{S1}$ and $\mathcal{N}_{S2}$, we need to correct the bias due to the difference of detection efficiencies in the two optical fibers in Fig.3 for selecting $\{1\}$ and $\{2\}$ states, respectively. We thus parameterize the overall efficiencies, $\epsilon_{1,2}$ for $\{1\}$ and $\{2\}$ states, respectively, as

$$\epsilon_1 \equiv \epsilon_{opt1}\epsilon_D, \qquad \epsilon_2 \equiv \epsilon_{opt2}\epsilon_D \tag{17}$$

where $\epsilon_{opt1,2}$ express optical collection efficiencies by the combination of the polarization beam splitter and optical fibers equipped with two lenses, and ϵ_D is the pure detection efficiency of the photomultiplier not including the optical paths (see the enlarged SPD part in Fig.3). What we directly measure experimentally is a branching ratio between two paths containing exactly the same optical components and the detector as those used for the pilot measurement, which corresponds to the ratio of these two efficiencies

$$B \equiv \frac{\epsilon_1}{\epsilon_2}. \tag{18}$$

This quantity is determined by taking the ratio between the numbers of photons in $T\{1\}$ and $T\{2\}$ at $\Theta = 90$ deg. and $\Theta = 0$ deg., respectively, in Fig.4. With B the acceptance-uncorrected photon numbers are expressed as

$$\mathcal{N}_{S1} = \frac{N_{S1}}{\epsilon_1} = \frac{N_{S1}}{B\epsilon_2} = \frac{N_{S1}}{B\epsilon_{opt2}\epsilon_D}, \qquad \mathcal{N}_{S2} = \frac{N_{S2}}{\epsilon_2} = \frac{N_{S2}}{\epsilon_{opt2}\epsilon_D}, \tag{19}$$

[2] The expected acceptance-uncorrected numbers of photons with $\{2\}$-state from atomic four-wave mixing processes are evaluated as $\sim 10^{-22}$ and $\sim 10^{-9}$ photons from the residual gas and optical elements for the same shot statistics as the present search, respectively, based on the supplementary measurements with higher intensity laser fields where four-wave mixing yields were evaluated as a function of residual gas pressures. We estimated these numbers of photons by scaling the results in the supplementary measurement down to the laser peak power of the two-color laser fields with the same optical elements and focusing geometry as the present search by taking differences of detector acceptances and shot statistics between the present search and the supplementary measurements into account.

where the second of Eq.(17) is substituted, and ϵ_D is known by the other measurement in advance.

As the second step, we evaluate the upper limit on the coupling-mass relation, where we regard the acceptance-uncorrected uncertainty δN_{S2} in the polarization state $\{2\}$ as the one standard deviation σ in the following Gaussian type of distribution with the mean value $\mu = N_{S2}$

$$1 - \alpha = \frac{1}{\sqrt{2\pi}\sigma} \int_{\mu-\delta}^{\mu+\delta} e^{-(x-\mu)^2/(2\sigma^2)} dx = \mathrm{erf}\left(\frac{\delta}{\sqrt{2}\sigma}\right), \tag{20}$$

where the estimator x corresponds to N_{S2} in our case, and the confidence level is given by $1 - \alpha$[14]. As the upper limit estimate, we apply $2\alpha = 0.05$ with $\delta = 2.24\sigma$ to give a confidence level of 95% in this analysis.

We then require that the expectation value of N_{S2} coincides with 2.24σ to obtain the upper limit at the 95% confidence level. In order to relate the upper limit on N_{S2} with the upper limit on the coupling-mass relation directly, we further need to deduce $\mathcal{N}_{S2}$ corresponding to the unbiased number of signal photons immediately after the focal point via the second of Eq.(19)

$$\mathcal{N}_{S2} = \frac{N_{S2}}{\epsilon_{opt2}\epsilon_D} = \frac{2.24\delta N_{S2}}{\epsilon_{opt2}\epsilon_D}. \tag{21}$$

Figure 8 shows the upper limit on the coupling-mass relation at the 95% confidence level which is calculated by requiring

$$W_s \mathcal{Y} = \mathcal{N}_{S2} \tag{22}$$

in Eq.(10) with the experimental parameters summarized in Tab.I and II. The excluded domain by this pilot search based on four-wave mixing (FWM) in QPS is indicated by the slantly shaded area. As references, we put existing upper limits by the other types of scalar field searches by vertically shaded areas: the ALPS experiment [15](the sine function part of the sensitivity curve is simplified by unity for the drawing purpose) which is one of the "Light Shinig through a Wall" (LSW) experiments, searching for non-Newtonian forces based on the torsion balance techniques (Etö-wash[16], Stanford1[17], Stanford2[18]) and the Casimir force measurement (Lamoreaux[19]). The domains below the vertically shaded areas are all excluded. We note that if we require the proper polarization combinations between initial and final states for pseudoscalar fields [7], we are able to test the QCD axion models in the near future. As a reference, we show the expected mass-coupling relation based on the QCD axion scenario for $E/N = 0$ [20] (KSVZ model [21]) which is indicated by the inclining

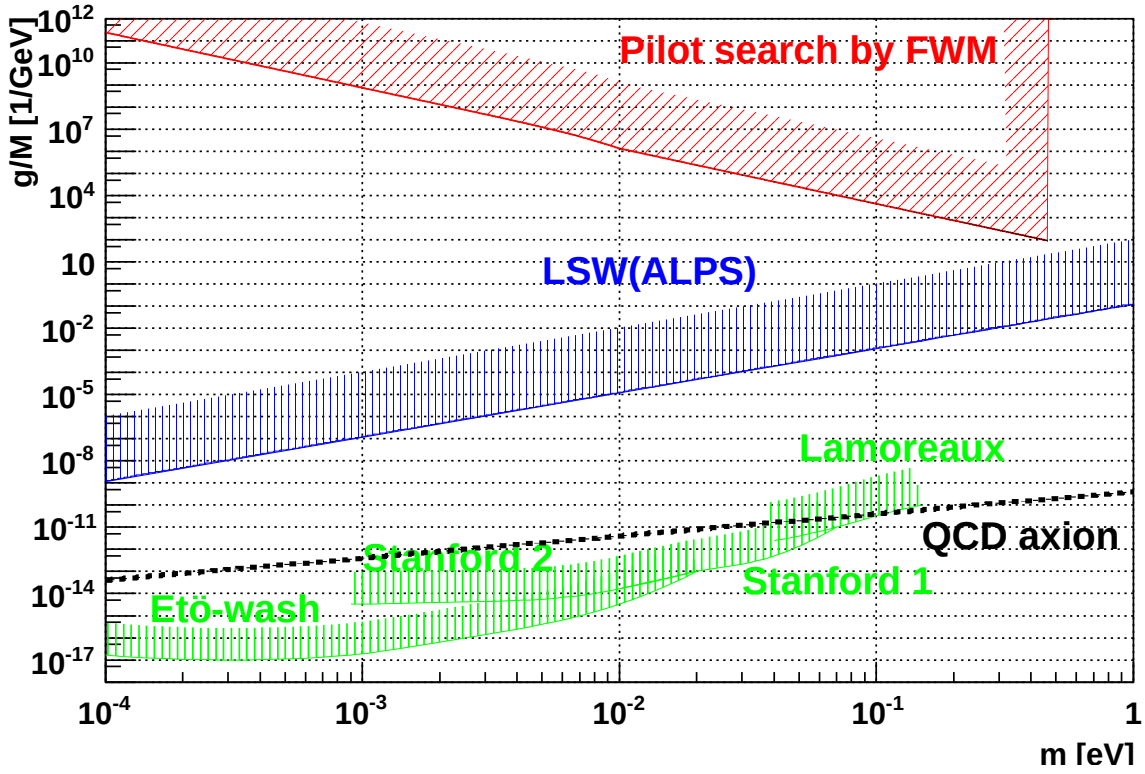

FIG. 8: Upper limits on the coupling g/M - mass m relation for the scalar field exchange. The excluded region by this pilot search based on four-wave mixing (FWM) in QPS is indicated by the slantly shaded area. The vertically shaded areas show the excluded regions by the other scalar field searches: the ALPS experiment [15](the sine function part of the sensitivity curve is simplified by unity for the drawing purpose) which is one of the "Light Shinig through a Wall" (LSW) experiments, searching for non-Newtonian forces based on the torsion balance techniques (Etö-wash[16], Stanford1[17], Stanford2[18]) and the Casimir force measurement (Lamoreaux[19]). As a reference for the future pseudoscalar searches, we also put the expected mass-coupling relation based on the QCD axion scenario for $E/N = 0$ [20] (KSVZ model [21]) indicated by the inclining dotted line.

dotted line.

VI. CONCLUSION

We demonstrated the pilot search for scalar fields in the mass region $m \leq 0.46$ eV via four-wave mixing of two-color laser fields. There is no significant four-wave mixing signals. We obtained the upper limit on the coupling-mass relation at a confidence level of 95%, which approximately follows $m^{-5/2}$ scaling with the highest sensitivity $g/M = 92.6$ GeV^{-1} at $m = 0.46$ eV. The concept of the experimental setup as well as the analysis procedure is extendable to higher intensity laser systems in the near future.

Appendix A: Re-evaluation of the signal yield

Given the formulae in Refs.[5–7] and the correction suggested by [22], we re-evaluate the signal yield with a more direct formulation than that based on the concept of *cross section*. The *cross section* is naturally applied to a beam flux normal to a target or the extension to head-on particle colliders where all beams are on the same axis. In QPS, however, this view point is not necessarily convenient due to the wide distribution of tilted incident fluxes. In such a case, we can adopt the more convenient formulation [23], which is useful, for instance, to evaluate the number of interactions in plasma where the concept of *a beam flux to a target* is no longer clear. With the notations in Fig.2 and the Lorentz invariant phase space factor dL_{ips}

$$dL_{ips} = (2\pi)^4 \delta(p_3 + p_4 - p_1 - p_2) \frac{d^3p_3}{2\omega_3(2\pi)^3} \frac{d^3p_4}{2\omega_4(2\pi)^3}, \tag{23}$$

the signal yield can be formulated as [23]

$$\begin{aligned} \mathcal{Y} &= \int dt d\vec{r} \rho_1(\vec{r}, t) \rho_2(\vec{r}, t) \int d\vartheta \frac{1}{2\omega 2\omega} \rho(\vartheta) |\mathcal{M}(\vartheta)|^2 dL_{ips} \\ &\equiv \mathcal{D}\left[s/L^3\right] \overline{\Sigma}\left[L^3/s\right], \end{aligned} \tag{24}$$

where $\mathcal{M}(\vartheta)$ is the Lorentz invariant transition amplitude as a function of incident angle ϑ with the normalized statistical weight $\rho(\vartheta)$ due to the uncertainty of the incident angle, $\mathcal{D}$ is time-integrated density and Σ is the interaction volume per unit time. We note the dimensions explicitly with time s and length L in [ ] of Eq.(24). On the other hand, it may be possible to factorize the yield based on the concept of *time-integrated luminosity* $\times$ *cross section* as follows

$$\mathcal{Y} = \int d\vartheta \rho(\vartheta) \left(\int dt d\vec{r} \rho_1(\vec{r}, t) \rho_2(\vec{r}, t) K(\vartheta) \right) \left(\frac{1}{K(\vartheta) 2\omega 2\omega} |\mathcal{M}(\vartheta)|^2 dL_{ips} \right)$$

$$\equiv \int d\vartheta \rho(\vartheta)\mathcal{L}(\vartheta)\left[s/(L^2\cdot s)\right]\sigma(\vartheta)\left[L^2\right], \tag{25}$$

where K corresponds to the relative velocity of incoming particle beams for a given ϑ based on the Møller's Lorentz invariant factor [25]. The relative velocity K is defined as [24]

$$K(\vartheta) \equiv \sqrt{(\vec{v_1}-\vec{v_2})^2 - \frac{(\vec{v_1}\times\vec{v_2})^2}{c^2}} = 2c\sin^2\vartheta, \tag{26}$$

with the notation in Fig.2. If $\rho(\vartheta)$ is a mere number, which is the normal case for collisions with two independent beams with a fixed relative velocity, this factorization is robust. In the case of the photon QPS, however, the concept of relative velocity between a pair of incident photons could be ambiguous due to spreads of single photon wavefunctions near the waist[3], while the squared scattering amplitude itself has to be averaged over a possible range on ϑ due to that unavoidable uncertainty. In order to recourse to the concept of a cross section, however, we need to choose a proper relative velocity value to convert a squared scattering amplitude into a cross section. We then face difficulty in uniquely determining a K-factor with respect to the averaged squared scattering amplitude over a range of ϑ in QPS. The formulation in Eq.(24) without recourse to the concept of a cross section, on the other hand, ambiguity originating from choices of a proper K-factor is all avoidable. Therefore, we re-formulate the signal yield based on Eq.(24) as follows.

We first express the squared scattering amplitude for the case when a low-mass field is exchanged in the s-channel via a resonance state with the symbol to describe polarization combinations of initial and final states S.

$$|\mathcal{M}_S|^2 \approx (4\pi)^2\frac{a^2}{\chi^2+a^2}, \tag{27}$$

where $\chi = \omega^2 - \omega_r^2$ with the resonance condition $m = 2\omega_r\sin\vartheta_r$ for a given mass m and a is expressed as

$$a = \frac{\omega_r^2}{8\pi}\left(\frac{gm}{M}\right)^2 = \frac{m\Gamma}{2\sin^2\vartheta_r} \tag{28}$$

with the resonance decay rate of the low-mass field [4]

$$\Gamma = (16\pi)^{-1}\left(gM^{-1}\right)^2 m^3. \tag{29}$$

[3] Our attitude might be strongly biased by the Copenhagen interpretation. If pre-existing momenta in advance of measurement could be realized in nature, it might allow us to explicitly define relative velocity. The approach expressed in Eq.(24), however, can circumvent this vague point originating from the different interpretations on *realism* in quantum mechanics.

[4] We note that if $M \sim M_{Planck} \sim 10^{18}$ GeV and $g \sim \alpha_{qed} \sim 10^{-2}$, the decay rate for $m \sim 10^{-9}$ GeV

The resonance condition is satisfied when the center-of-mass system (CMS) energy between incident two photons $E_{CMS} = 2\omega \sin\vartheta$ coincides with the given mass m. At a focused geometry of an incident laser beam, however, E_{CMS} cannot be uniquely specified due to the momentum uncertainty of incident waves. Although the incident laser energy has the intrinsic uncertainty, the momentum uncertainty or the angular uncertainty between a pair of incident photons dominates that of the incident energy. Therefore, we consider the case where only angles of incidence ϑ between randomly chosen pairs of photons are uncertain within $0 < \vartheta \leq \Delta\vartheta$ for a given focusing parameter by fixing the incident energy. The treatment for the intrinsic energy uncertainty is explained in Appendix B later. We fix the laser energy ω at the optical wavelength

$$\omega_{opt}^2 = \frac{m^2}{4\vartheta_r^2} \sim 1\mathrm{eV}^2, \tag{30}$$

while the resonance condition depends on the incident angle uncertainty. This gives the expression for χ as a function of ϑ

$$\chi(\vartheta) = w_{opt}^2 - w_r^2(\vartheta) = \frac{m^2}{4\vartheta_r^2} - \frac{m^2}{4\vartheta^2} = \left(1 - (\vartheta_r/\vartheta)^2\right)\omega_{opt}^2, \tag{31}$$

where

$$d\vartheta = \frac{\vartheta_r}{2\omega_{opt}^2}(1 - \frac{\chi}{\omega_{opt}^2})^{-3/2} d\chi. \tag{32}$$

We thus introduce the averaging process for the squared amplitude $\overline{|\mathcal{M}_S|^2}$ over the possible uncertainty on incident angles

$$\overline{|\mathcal{M}_S|^2} = \int_0^{\pi/2} \rho(\vartheta)|\mathcal{M}_S(\vartheta)|^2 d\vartheta \tag{33}$$

where $\mathcal{M}_S$ specified with a set of physical parameters m and gM^{-1} is expressed as a function of ϑ, and $\rho(\vartheta)$ is the probability distribution function as a function of the uncertainty on ϑ within an incident pulse.

We review the expression for the electric field of the Gaussian laser propagating along the z-direction in spatial coordinates (x, y, z) [9] as follows:

$$\vec{E}(x, y, z) = \vec{E}_0$$

becomes $\sim 10^{-41}$ Hz, hence, the lifetime is quite long. Therefore, we need to stimulate the decay at the same time as the production by supplying an inducing laser field in advance of the interaction, that is, we treat the interaction as an instantaneous scattering process where the production and the decay cannot be distinguished in spacetime.

$$\frac{w_0}{w(z)} \exp\left\{-i[kz - H(z)] - r^2\left(\frac{1}{w(z)^2} + \frac{ik}{2R(z)}\right)\right\}, \tag{34}$$

where E_0 electric field amplitude, $k = 2\pi/\lambda$, $r = \sqrt{x^2 + y^2}$, w_0 is the minimum waist, which cannot be smaller than λ due to the diffraction limit, and other definitions are as follows:

$$w(z)^2 = {w_0}^2\left(1 + \frac{z^2}{{z_R}^2}\right), \tag{35}$$

$$R = z\left(1 + \frac{{z_R}^2}{z^2}\right), \tag{36}$$

$$H(z) = \tan^{-1}\left(\frac{z}{z_R}\right), \tag{37}$$

$$z_R \equiv \frac{\pi {w_0}^2}{\lambda}. \tag{38}$$

With θ being an incident angle of a single photon in the Gaussian beam, the angular distribution $g(\theta)$ can be approximated as

$$g(\theta) \sim \frac{1}{\sqrt{2\pi}\Delta\theta} \exp\left\{-\frac{\theta^2}{2\Delta\theta^2}\right\}, \tag{39}$$

where the incident angle uncertainty in the Gaussian beam $\Delta\theta$ is introduced within the physical range $|\theta| < \pi/2$ as

$$\Delta\theta \sim \frac{\lambda_c}{\pi w_0} = \frac{d}{2f}, \tag{40}$$

with the wavelength of the creation laser λ_c, the beam diameter d, the focal length f, and the beam waist $w_0 = \frac{f\lambda_c}{\pi d/2}$ as illustrated in Fig.1. For a pair of photons 1, 2 each of which follows $g(\theta)$, the incident angle between them is defined as

$$\vartheta = \frac{1}{2}|\theta_1 - \theta_2|. \tag{41}$$

With the variance $\Delta\vartheta^2 = 2(\frac{1}{4}\Delta\theta^2)$, the pair angular distribution $\rho(\vartheta)$ is then approximated as

$$\rho(\vartheta) \sim \frac{2}{\sqrt{\pi}\Delta\theta} \exp\left\{-\left(\frac{\vartheta}{\Delta\theta}\right)^2\right\} \sim \frac{2}{\sqrt{\pi}\Delta\theta} \quad \text{for} \quad 0 < \vartheta < \pi/2 \tag{42}$$

where the coefficient 2 of the amplitude is caused by limiting ϑ to the range $0 < \vartheta < \pi/2$, and $\left(\frac{\vartheta}{\Delta\theta}\right)^2 \ll 1$ is taken into account because $\Delta\theta$ in Eq.(40) also corresponds to the upper

limit by the focusing lens based on geometric optics. This distribution is consistent with the flat top distribution applied to Ref.[6, 7] except the coefficient.

We now re-express the average of the squared scattering amplitude as a function of $\chi \equiv a\xi$ in units of the width of the Breit-Wigner(BW) distribution a by substituting Eq.(27) and (42) into Eq.(33) with Eq.(32)

$$\overline{|\mathcal{M}_S|^2} = \frac{(4\pi)^2}{\sqrt{\pi}\omega_{opt}^2}\left(\frac{\vartheta_r}{\Delta\theta}\right) a\mathcal{W}, \tag{43}$$

where we introduce the following constant

$$\mathcal{W} \equiv \int_{-\infty}^{\frac{\omega_{opt}^2}{a}\{1-(\vartheta_r/(\pi/2))^2\}} W(\xi)\frac{1}{\xi^2+1}d\xi \tag{44}$$

with

$$W(\xi) \equiv (1-\frac{a\xi}{\omega_{opt}^2})^{-3/2}. \tag{45}$$

In Eq.(44) the weight function $W(\xi)$ is the positive and monotonic function within the integral range and the second term is the Breit-Wigner(BW) function with the width of unity. Note that $\overline{|\mathcal{M}_S|^2}$ is now explicitly proportional to a but not a^2. This gives the enhancement factor a compared to the case $\overline{|\mathcal{M}_S|^2} \propto a^2$ where no resonance state is contained in the integral range controlled by $\Delta\theta$ experimentally. The integrated value of the pure BW function from $\xi = -1$ to $\xi = +1$ gives $\pi/2$, while that from $\xi = -\infty$ to $\xi = +\infty$ gives π. The difference is only a factor of two. The weight function $W(\xi)$ of the kernel is almost unity for small $a\xi$, that is, when a is small enough with a small mass and a weak coupling. For instance, in the coupling-mass range covered by Fig.8, $g/M \sim 10^{11}$ GeV^{-1} and $m \sim 10^{-13}$ GeV gives $a \sim 10^{-5}$, while $g/M \sim 10^2$ GeV^{-1} and $m \sim 10^{-10}$ GeV gives $a \sim 10^{-17}$. In such cases the integrated value of Eq.(44) is close to that of BW, because the weight function is close to unity and also the upper limit of the integral range in Eq.(44) is large for $\vartheta_r/\Delta\vartheta < 1$ by the a^{-1} dependence. In Ref.[7], we thus approximate $\mathcal{W}$ as $\pi/2$ for the conservative estimate.

Let us remind of the partially integrated cross section over the solid angle of the signal photon ω_3 which corresponds to Eq.(11) in Ref.[7]. The expression before taking the average over ϑ, hence as a function of ϑ, is as follows

$$\sigma(\vartheta) = \frac{\mathcal{F}_S|\mathcal{M}_S(\vartheta)|^2}{(8\pi\omega)^2\sin^4\vartheta}\int_{\underline{\theta_3}}^{\overline{\theta_3}}\left(\frac{\omega_3}{2\omega}\right)^2\sin\theta_3 d\theta_3. \tag{46}$$

We then convert the interaction cross section $\sigma(\vartheta)$ into the interaction volume per unit time $\Sigma(\vartheta)$ by simply multiplying the relative velocity $K(\vartheta) = 2c\sin^2\vartheta$

$$\Sigma(\vartheta) = \frac{2c\mathcal{F}_S|\mathcal{M}_S(\vartheta)|^2}{(8\pi\omega)^2\sin^2\vartheta}\int_{\underline{\theta_3}}^{\overline{\theta_3}}\left(\frac{\omega_3}{2\omega}\right)^2\sin\theta_3 d\theta_3 \sim \frac{2c^3\mathcal{F}_S|\mathcal{M}_S(\vartheta)|^2}{(8\pi)^2}\left(\frac{\lambda_c}{2\pi c}\right)^2\frac{\delta u}{4} \quad \left[L^3/s\right] \quad (47)$$

where the creation laser wavelength λ_c, $\delta u \equiv \overline{u} - \underline{u}$ with approximations $u^2 \ll 1$ and $\vartheta \ll 1$, and c and $\hbar$ are restored to confirm the dimension explicitly. The averaged value over ϑ is then expressed as

$$\begin{aligned}
\overline{\Sigma} &= \int_0^{\pi/2} d\vartheta\rho(\vartheta)\Sigma(\vartheta) = \frac{c\mathcal{F}_S\lambda_c^2\delta u}{2(16\pi^2)^2}\int_0^{\pi/2} d\vartheta\rho(\vartheta)|\mathcal{M}_S(\vartheta)|^2 \\
&\sim \frac{c\mathcal{F}_S\lambda_c^2\delta u}{2(16\pi^2)^2}\frac{(4\pi)^2}{\sqrt{\pi}\omega_{opt}^2}\left(\frac{\vartheta_r}{\Delta\theta}\right)a\mathcal{W} = \frac{c\mathcal{W}\mathcal{F}_S\lambda_c^2\delta u}{2\sqrt{\pi}(4\pi)^2\omega_{opt}^2}\left(\frac{\vartheta_r}{\Delta\theta}\right)a \\
&= \frac{c\mathcal{W}\mathcal{F}_S\lambda_c^2\delta u}{2\sqrt{\pi}(4\pi)^2\omega_{opt}^2}\left(\frac{\vartheta_r}{\Delta\theta}\right)\frac{\omega_r^2}{8\pi}\left(\frac{gm}{M}\right)^2 \\
&= \frac{c\mathcal{W}\mathcal{F}_S\lambda_c^2\delta u}{4\sqrt{\pi}(4\pi)^3}\left(\frac{\vartheta_r}{\Delta\theta}\right)\left(\frac{gm}{M}\right)^2, \qquad (48)
\end{aligned}$$

where Eq.(43) and a in Eq.(28) are substituted in the second and third lines, respectively, and $\omega_r \equiv \omega_{opt}$ via Eq.(30) is identified for the last line.

We now consider the time-integrated density factor $\mathcal{D}$ in Eq.(24) applicable to free propagation of the Gaussian laser beam for creation as illustrated in Fig.1. We first parameterize the density profile of an incident Gaussian laser beam being the focal point at $z = 0$ with the pulse duration time τ_c propagating over the focal length f along z-axis as [26]

$$\rho_c(x,y,z,t) = \frac{2N_c}{\pi w^2(z)}\exp\left\{-2\frac{x^2+y^2}{w^2(z)}\right\}\frac{1}{\sqrt{\pi}c\tau_c}\exp\left\{-\left(\frac{z'}{c\tau_c}\right)^2\right\}, \quad (49)$$

where the central position of the creation pulse in z coordinate is traced by the relation $z = ct$ as a function of time t while the pulse duration along z-direction is expressed with the local coordinate z', hence, $z' = z - ct$, and N_c is the average number of creation photons per pulse. Using the squared expression

$$\rho_c^2(x,y,z,t) = \frac{4{N_c}^2}{\pi^3(c\tau_c)^2}\frac{1}{w^4(z)}\exp\left\{-4\frac{x^2+y^2}{w^2(z)}\right\}\exp\left\{-2\left(\frac{z'}{c\tau_c}\right)^2\right\} \quad (50)$$

based on Eq.(24), $\mathcal{D}_c$ is then expressed as

$$\mathcal{D}_c = \int_{-f/c}^{0} dt\int_{-\infty}^{\infty} dx\int_{-\infty}^{\infty} dy\int_{-\infty}^{\infty} dz{\rho_c}^2(x,y,z,t)$$

$$
\begin{aligned}
&= \frac{4N_c^2}{\pi^3(c\tau_c)^2}\int_{-f/c}^{0} dt \frac{1}{w^4(ct)}\sqrt{\frac{\pi w^2(ct)}{4}}\sqrt{\frac{\pi w^2(ct)}{4}}\int_{-\infty}^{\infty} dz^{'} \exp\left\{-2\left(\frac{z^{'}}{c\tau_c}\right)^2\right\} \\
&= \frac{N_c^2}{\sqrt{2\pi}}\frac{1}{\pi {w_0}^2}\frac{1}{c\tau_c}\int_{-f/c}^{0} dt \frac{1}{1+(ct/z_R)^2} \\
&= \frac{N_c^2}{\sqrt{2\pi}}\frac{1}{\pi {w_0}^2}\frac{1}{c\tau_c}\frac{z_R}{c}\tan^{-1}\left(\frac{f}{z_R}\right) \quad \left[s/L^3\right], \qquad (51)
\end{aligned}
$$

where the time integration is performed during the pulse propagation from $z = -f$ to $z = 0$, because the photon-photon scattering never take place when two photons in a pair are apart from each other at $z > 0$.

We now evaluate the effect of the inducing laser beam. The inducing effect is expected only when p_4 as a result of scattering coincides with a photon momentum included in the coherent state of the inducing beam. In order to characterize p_4 from the interaction, we first summarize the kinematic relations specified in Fig.2. Although the CMS-energy varies depending on the incident angle ϑ, the interaction rate is dominated at the CMS-energy satisfying the resonance condition $E_{CMS} = m = 2\omega \sin\vartheta_r$ via the Breit-Wigner weighting. Therefore, p_4 is essentially expressed with the condition $\vartheta = \vartheta_r$ in Eq.(7). With $\vartheta_r \ll 1$, we obtain following relations

$$
\theta_4 \sim \mathcal{R}^{-1/2}\vartheta_r \quad \text{and} \quad \theta_3 \sim \mathcal{R}^{1/2}\vartheta_r. \qquad (52)
$$

These relations imply that the spontaneous interaction causes ring-like patterns of emitted photons with cone angles θ_3 and θ_4 commonly constrained by ϑ_r, because the way to take a reaction plane determined by $p_{1,2,3,4}$ is symmetric around the z-axis.

We then evaluate how much fraction of photon momenta in the inducing beam overlaps with the p_4, in other words, the acceptance factor applied to the ideal Gaussian laser beam, which was discussed within the plane wave approximation in [7]. In the beam waist at $z = 0$, the angular spectrum representation gives the following electric field distribution as a function of wave vector components k_x and k_y on the transverse plane $z = 0$ based on Fourier transform of $\vec{E}(x, y, z = 0)$ [27]

$$
\vec{E}(k_x, k_y; z = 0) = \vec{E_0}\frac{w_0^2}{4\pi}e^{-\frac{w_0^2}{4}(k_x^2+k_y^2)} \equiv \vec{E_0}\frac{w_0^2}{4\pi}e^{-\frac{w_0^2}{4}k_T^2}, \qquad (53)
$$

where the transverse wave vector component $k_T^2 = k_x^2 + k_y^2$ is introduced. With the paraxial approximation $k_z \sim k - k_T^2/2k$, we can derive exactly the same expression for $E(x, y, z)$ in Eq.(34) starting from this representation[27]. We apply Eq.(53) to the inducing beam

represented by the subscript 4 with $k_{T4} \equiv k_4 \sin\theta_4 \sim k_4 \mathcal{R}^{-1/2}\vartheta_r$ using the first in Eq.(52) and $w_{04} \equiv \frac{f\lambda_i}{\pi d/2}$. For a range from $\underline{k_{T4}}$ to $\overline{k_{T4}}$ by denoting the underline and overline as the lower and upper values on the corresponding variables, the acceptance factor $\mathcal{A}_i$ is estimated as

$$\begin{aligned}
\mathcal{A}_i &\equiv \frac{\int_{\underline{k_{T4}}}^{\overline{k_{T4}}} 2\pi k_{T4} E_4^2 dk_{T4}}{\int_0^\infty 2\pi k_{T4} E_4^2 dk_{T4}} = e^{-\frac{w_{04}^2}{2}\underline{k_{T4}}^2} - e^{-\frac{w_{04}^2}{2}\overline{k_{T4}}^2} \sim \frac{w_{04}^2}{2}(\overline{k_{T4}}^2 - \underline{k_{T4}}^2) \\
&\sim \frac{w_{04}^2 k_4^2}{2}\vartheta_r^2(\underline{\mathcal{R}}^{-1} - \overline{\mathcal{R}}^{-1}) \\
&\sim 2(\underline{\mathcal{R}}^{-1} - \overline{\mathcal{R}}^{-1})\left(\frac{\vartheta_r}{\Delta\theta}\right)^2 = 4\delta\mathcal{U}\left(\frac{\vartheta_r}{\Delta\theta}\right)^2, \qquad (54)
\end{aligned}$$

where the approximation in the first line is based on $w_{04}k_{T4} \ll 1$, $k_{T4} \sim k_4\mathcal{R}^{-1/2}\vartheta_r$ is substituted in the second line, and $w_{04}k_4 = \frac{2\pi w_{04}}{\lambda_i} \equiv 2/\Delta\theta_4$ with $\Delta\theta_4 \sim \Delta\theta$ due to the common focusing geometry d and f to those of the creation beam is substituted in the third line by defining $\delta\mathcal{U} \equiv \frac{\overline{u}-\underline{u}}{\overline{u}\,\underline{u}}$. We note that Eq.(54) now has the quadratic dependence on ϑ_r while the corresponding acceptance factor in [7] was proportional to ϑ_r due to the plane wave approximation.

Because of the common optical element sharing the same optical axis, in advance, the spatial overlap between creation and inducing lasers is satisfied in QPS. In actual experiments, however, it is likely that the time durations between the two laser pulses are prepared as $\tau_i \geq \tau_c$ for inducing i and creation c beams, respectively, because shortness of τ_c is more important to enhances $\mathcal{D}_c$ via the quadratic nature on the pulse energy. Therefore, we further introduce a factor representing the spacetime overlap by assuming the pulse peaks in spacetime coincide with each other. Hence, the entire inducing effect is expressed as

$$\mathcal{I} = \mathcal{A}_i\left(\frac{\tau_c}{\tau_i}\right)N_i = 4\delta\mathcal{U}\left(\frac{\vartheta_r}{\Delta\theta}\right)^2\left(\frac{\tau_c}{\tau_i}\right)N_i. \qquad (55)$$

Therefore, the overall density factor $\mathcal{D}_{c+i}$ including the inducing laser effect is expressed as

$$\begin{aligned}
\mathcal{D}_{c+i} &\sim C_{mb}\mathcal{D}_c\mathcal{I} \\
&= C_{mb}\frac{N_c^2}{\sqrt{2\pi}}\frac{1}{\pi {w_0}^2}\frac{1}{c\tau_c}\frac{z_R}{c}\tan^{-1}\left(\frac{f}{z_R}\right)4\delta\mathcal{U}\left(\frac{\vartheta_r}{\Delta\theta}\right)^2\left(\frac{\tau_c}{\tau_i}\right)N_i \\
&= \frac{4}{\sqrt{2\pi}}\frac{z_R}{\pi {w_0}^2 c^2\tau_c}\left(\frac{\tau_c}{\tau_i}\right)\tan^{-1}\left(\frac{f}{z_R}\right)\left(\frac{\vartheta_r}{\Delta\theta}\right)^2\delta\mathcal{U}C_{mb}N_c^2N_i \\
&= \frac{4}{\sqrt{2\pi}}\frac{1}{c^2\lambda_c\tau_c}\left(\frac{\tau_c}{\tau_i}\right)\tan^{-1}\left(\frac{\pi d^2}{4\ f\lambda_c}\right)\left(\frac{\vartheta_r}{\Delta\theta}\right)^2\delta\mathcal{U}C_{mb}N_c^2N_i \qquad (56)
\end{aligned}$$

where $C_{mb} = 1/2$ corresponds to the combinatorial factor originating from the choice of a frequency among the frequency multimode states in creation and inducing lasers as discussed in Ref.[7].

Based on Eq.(24) with Eqs.(48) and (56), the re-evaluated signal yield $\mathcal{Y}$ is finally expressed as

$$\begin{aligned}
\mathcal{Y} &= \mathcal{D}_{c+i}\overline{\Sigma} \\
&= \frac{4}{\sqrt{2\pi}}\frac{1}{c^2\lambda_c\tau_c}\left(\frac{\tau_c}{\tau_i}\right)\tan^{-1}\left(\frac{\pi d^2}{4\ f\lambda_c}\right)\left(\frac{\vartheta_r}{\Delta\theta}\right)^2\delta\mathcal{U}C_{mb}N_c^2N_i\frac{c\mathcal{W}\mathcal{F}_S\lambda_c^2\delta u}{4\sqrt{\pi}(4\pi)^3}\left(\frac{\vartheta_r}{\Delta\theta}\right)\left(\frac{gm}{M}\right)^2 \\
&= \frac{1}{\sqrt{2}\pi(4\pi)^3}\left(\frac{\lambda_c}{c\tau_c}\right)\left(\frac{\tau_c}{\tau_i}\right)\tan^{-1}\left(\frac{\pi d^2}{4\ f\lambda_c}\right)\left(\frac{\vartheta_r}{\Delta\theta}\right)^3\delta u\delta\mathcal{U}\left(\frac{gm}{M}\right)^2\mathcal{W}\mathcal{F}_SC_{mb}N_c^2N_i \\
&= \frac{1}{\sqrt{2}\pi(4\pi)^3}\left(\frac{\lambda_c}{c\tau_c}\right)\left(\frac{\tau_c}{\tau_i}\right)\Delta\theta^{-3}\tan^{-1}\left(\frac{\pi d^2}{4\ f\lambda_c}\right)\delta u\delta\mathcal{U}\left(\frac{gm}{M}\right)^2\left(\frac{m}{2\omega[eV]}\right)^3\mathcal{W}\mathcal{F}_SC_{mb}N_c^2N_i \\
&\sim \frac{1}{64\sqrt{2}\pi^4}\left(\frac{\lambda_c}{c\tau_c}\right)\left(\frac{\tau_c}{\tau_i}\right)\left(\frac{f}{d}\right)^3\tan^{-1}\left(\frac{\pi d^2}{4\ f\lambda_c}\right)\frac{(\overline{u}-\underline{u})^2}{\overline{u}\underline{u}}\left(\frac{gm[eV]}{M[eV]}\right)^2\left(\frac{m[eV]}{\omega[eV]}\right)^3\mathcal{W}\mathcal{F}_SC_{mb}N_c^2N_i,
\end{aligned} \tag{57}$$

where the parameters specified with [eV] apply natural units. We note that the re-evaluated signal yield depends on m^5 compared to the m^2 dependence in Ref.[7]. The additional m^2 dependence is caused by multiplying K-factor in Eq.(47) and the m dependence is further added by Eq.(54) due to the ring-image acceptance for the inducing effect. The sensitivity to lower mass domains thus diminishes.

Appendix B: The effect of finite spectrum widths of creation and inducing laser beams

When creation and inducing lasers have finite spectrum widths, the effect has impacts on the interaction rate of four-wave mixing as well as the spectrum width of the signal via energy-momentum conservation within the unavoidable uncertainty of photon momenta and energies in QPS. We have considered the effect of the finite line width of the inducing laser field by assuming the line width of the creation laser is negligibly small [7]. In such a case, the energy uncertainties in the process of four-wave mixing with the convention used in Fig.2 are described as

$$\omega = \langle\omega\rangle, \quad \omega_4 = \langle\omega_4\rangle \pm \delta\omega_4, \quad \text{and} \quad \omega_3 = \langle\omega_3\rangle \pm \delta\omega_3 \tag{58}$$

for the creation laser, the inducing laser, and the signal, respectively, where $\langle\cdot\cdot\rangle$ denotes average of each spectrum, $\delta\omega_4$ expresses the intrinsic line width caused by the energy uncertainty in the atomic process to produce the inducing laser beam, and $\delta\omega_3 = \delta\omega_4$ arises due to the energy conservation [7].

In this case $\overline{u}$ and $\underline{u}$ in Eq.(57) via Eq.(3) solely originates from the intrinsic line width of the inducing laser field. However, this approximation is not valid for the case where the line width of the creation laser is equal to or wider than that of the inducing laser. We now provide the prescription for the following general case:

$$\omega = \langle\omega\rangle + \delta\omega, \quad \omega_4 = \langle\omega_4\rangle \pm \delta\omega_4, \quad \text{and} \quad \omega_3 = \langle\omega_3\rangle \pm \delta\omega_3, \tag{59}$$

where the intrinsic line width of the creation laser $\delta\omega$ is explicitly included. In this case, at a glance, Eq.(6) must be modified so that a finite net transverse momentum along the x-axis in Fig.2 is introduced by the different incident photon energies ω_1 and ω_2 with corresponding incident angles ϑ_1 and ϑ_2, respectively. These notations are for a *nominal* laboratory frame defined by a pair of asymmetric incident photons, referred to as L-system. Here *nominal* implies that we cannot specify individual photon's incident wavelength as well as incident angle physically, that is, what we know *a priori* is only the ranges of uncertainties on possible wavelengths and incident angles. Exactly speaking, all the calculations so far are based on the equal incident energy $\langle\omega\rangle$ with the equal incident angle ϑ in the averaged laboratory frame, referred to as $\langle L\rangle$-system as illustrated in Fig.2, where the transverse momentum of the incident colliding system is zero on the average. We regard the effect of these *nominally* possible L-systems as fluctuations around the averaged $\langle L\rangle$-system We, therefore, attempt to transform L-systems into a $\langle L\rangle$-system so that $\delta\omega$ is effectively invisible as follows

$$\omega = \langle\omega\rangle, \quad \omega_4 = \langle\omega_4\rangle \pm \Delta\omega_4, \quad \text{and} \quad \omega_3 = \langle\omega_3\rangle \pm \Delta\omega_3, \tag{60}$$

where $\delta\omega$ in Eq.(59) is absorbed into the effective line widths of the final state photon energies in the $\langle L\rangle$-system resulting in $\Delta\omega_4 > \delta\omega_4$ denoting Δ as the effective width in the $\langle L\rangle$-system and accordingly $\Delta\omega_3 > \delta\omega_3$ arises via energy-momentum conservation in that system.

As long as a resonance state with a finite mass is formed, a range $0 < \vartheta \leq \Delta\vartheta$ in Fig.1 eventually contains the resonance angle ϑ_r which satisfies the condition that the center-of-mass system energy $E_{CMS} = 2\langle\omega\rangle \sin\vartheta_r$ coincides with the mass m in the $\langle L\rangle$-system, and

any *nominal* L-systems which satisfy the resonance condition can be generally formed by a transverse Lorentz boost of the $\langle L\rangle$-system with the relative velocity β with respect to the velocity of light c. Assigning the positive direction of β to the positive direction of x-axis in Fig.2, the energy and the transverse momentum relations between a L-system and the $\langle L\rangle$-system are connected via [13]

$$\begin{pmatrix} \omega_1 \\ p_{1T} \end{pmatrix} = \gamma \begin{pmatrix} 1 & -\beta \\ -\beta & 1 \end{pmatrix} \begin{pmatrix} \langle\omega\rangle \\ \langle\omega\rangle \sin\vartheta \end{pmatrix},$$
$$\begin{pmatrix} \omega_2 \\ p_{2T} \end{pmatrix} = \gamma \begin{pmatrix} 1 & -\beta \\ -\beta & 1 \end{pmatrix} \begin{pmatrix} \langle\omega\rangle \\ -\langle\omega\rangle \sin\vartheta \end{pmatrix} \tag{61}$$

with $\gamma \equiv (1-\beta^2)^{-1/2}$, where the subscripts 1 and 2 correspond to the photon indices in Fig.2, respectively. Since the relations of the energy components in Eq.(61) indicate that p_1 experiences frequency-down shift, while p_2 does frequency-up shift, we introduce another definitions of energy components of p_1 and p_2 after the transverse boost by

$$\omega_1 = \gamma\langle\omega\rangle(1-\beta\sin\vartheta) \equiv \langle\omega\rangle - \delta\omega \equiv \langle\omega\rangle\,(1-\delta r)\,,$$
$$\omega_2 = \gamma\langle\omega\rangle(1+\beta\sin\vartheta) \equiv \langle\omega\rangle + \delta\omega \equiv \langle\omega\rangle\,(1+\delta r) \tag{62}$$

where a relative line width with respect to the mean energy of the creation laser $\delta r \equiv \delta\omega/\langle\omega\rangle$ is implemented. We note the following physical and experimental conditions:

$$0 < \beta < 1 \quad \text{and} \quad 0 < \delta r \ll 1, \tag{63}$$

respectively. For convenience, we tentatively distinguish β for $\omega_{1,2}$ by the subscripts in the following discussion.

As for ω_1, from the first of Eq.(62) with $\delta r \ll 1$, we obtain the following equation

$$(1+\sin^2\vartheta - 2\delta r)\beta_1^2 - 2\sin\vartheta\beta_1 + 2\delta r = 0 \tag{64}$$

with the solutions by assuming $\vartheta \ll 1$

$$\beta_{1\pm} \equiv \frac{\vartheta \pm \sqrt{D_1}}{1+\vartheta^2-2\delta r} \sim (1-\vartheta^2+2\delta r)\left(\vartheta \pm \sqrt{D_1}\right), \tag{65}$$

where

$$D_1 \sim \vartheta^2 - (1+\vartheta^2-2\delta r)2\delta r \sim \vartheta^2 - 2\delta r. \tag{66}$$

Requiring $D_1 \geq 0$ gives a physical constraint

$$2\delta r \leq \vartheta^2. \tag{67}$$

If this is satisfied, $\sqrt{D_1} \sim (\vartheta^2 - 2\delta r)^{1/2} \sim \vartheta - \delta r/\vartheta$ with $\delta r \ll 1$ gives

$$\vartheta \pm \sqrt{D_1} \sim \vartheta \pm \left(\vartheta - \frac{\delta r}{\vartheta}\right). \tag{68}$$

The double-sign symbol in Eq.(65) gives following two solutions:

$$\begin{aligned} \beta_{1+} &\sim (1 - \vartheta^2 + 2\delta r)\left(2\vartheta - \frac{\delta r}{\vartheta}\right) \sim 2\vartheta - \frac{\delta r}{\vartheta}, \\ \beta_{1-} &\sim (1 - \vartheta^2 + 2\delta r)\left(\frac{\delta r}{\vartheta}\right) \sim \frac{\delta r}{\vartheta} > 0, \end{aligned} \tag{69}$$

where only β_{1-} is physically acceptable, while β_{1+} is not, because the limit of $\delta r \to 0$ must correspond to $\beta = 0$ in our discussion.

Let us move on to discuss ω_2. From the second of Eq.(62) with $\delta r \ll 1$, we get

$$(1 + \sin^2\vartheta + 2\delta r)\beta_2^2 + 2\sin\vartheta\beta_2 - 2\delta r = 0 \tag{70}$$

with the solutions by assuming $\vartheta \ll 1$

$$\beta_{2\pm} \equiv \frac{-\vartheta \pm \sqrt{D_2}}{1 + \vartheta^2 + 2\delta r} \sim (1 - \vartheta^2 - 2\delta r)\left(-\vartheta \pm \sqrt{D_2}\right), \tag{71}$$

where

$$D_2 \sim \vartheta^2 + (1 + \vartheta^2 + 2\delta r)2\delta r \sim \vartheta^2 + 2\delta r > 0. \tag{72}$$

The approximation $\sqrt{D_2} \sim (\vartheta^2 + 2\delta r)^{1/2} \sim \vartheta + \delta r/\vartheta$ with $\delta r \ll 1$ gives

$$-\vartheta \pm \sqrt{D_2} \sim -\vartheta \pm \left(\vartheta + \frac{\delta r}{\vartheta}\right). \tag{73}$$

The double-sign symbol in Eq.(71) gives following two solutions:

$$\begin{aligned} \beta_{2+} &\sim (1 + \vartheta^2 + 2\delta r)\left(\frac{\delta r}{\vartheta}\right) \sim \frac{\delta r}{\vartheta} > 0, \\ \beta_{2-} &\sim (1 + \vartheta^2 + 2\delta r)\left(-2\vartheta - \frac{\delta r}{\vartheta}\right) \sim -2\vartheta - \frac{\delta r}{\vartheta}, \end{aligned} \tag{74}$$

where only β_{2+} is physically acceptable, while β_{2-} is not due to the same reason as ω_1 in addition to the positivity condition.

A common β is eventually determined as

$$\beta \sim \beta_{1-} = \beta_{2+} = \frac{\delta r}{\vartheta} \tag{75}$$

based on Eqs.(69) and (74). By substituting δr in Eq.(75) into Eq.(67), the range of β is expressed as

$$\beta < \frac{\vartheta}{2}. \tag{76}$$

Among ϑ within $\Delta\vartheta$, ϑ_r is effectively enhanced based on the Breit-Wigner distribution in the averaging process of the square of the invariant scattering amplitude around $E_{CMS} = 2\sin\vartheta_r\langle\omega\rangle$ [6]. Therefore, for a given mass $m \sim 2\langle\omega\rangle\vartheta_r$ with $\vartheta_r \ll 1$, the effective physical limit on β is expressed as

$$\beta_r \equiv \frac{\delta r}{\vartheta_r} < \frac{\vartheta_r}{2}. \tag{77}$$

On the other hand, an instrumental full line width of a creation laser $\Delta r \equiv \delta\omega_{full}/\langle\omega\rangle$ is given by the creation laser intrinsically. Therefore, the range of β can be maximally covered by

$$0 < \beta < \beta_c \equiv \frac{\Delta r}{\vartheta} \tag{78}$$

based on the relation in Eq.(75). If β_c is smaller than β_r, however, the instrumental condition limits β to $\beta \leq \beta_c$ before reaching the physical limit β_r for a given mass parameter. Therefore, we are required to choose smaller β, either β_c or β_r, depending on the relation between an experimentally given line width of the creation laser and a given mass parameter we search for.

Given a possible range of β based on the relation between an intrinsic line width of the creation laser and a given mass m, we can construct a unique $\langle L\rangle$-system by inversely boosting individual L-systems, where the intrinsic line width $\delta\omega_4$ is effectively broaden. This is because a spectrum width is effectively embedded by the possible range of inverse boosts for a ω_4 chosen among $\langle\omega_4\rangle - \delta\omega_4 \leq \omega_4 \leq \langle\omega_4\rangle + \delta\omega_4$ in individual L-systems. Therefore, combining the inverse-boost-originating spectrum width with the intrinsic line width of the inducing laser provides the effective inclusive range of u defined in Eq.(3) in the $\langle L\rangle$-system.

We first evaluate how much the common inverse boost originating from the line width of the creation laser solely changes the range of u from $\underline{u}_c$ to $\overline{u}_c$ in the $\langle L\rangle$-system for a ω_4 within the line width of the inducing laser field. By inversely applying the boost in Eq.(61)

to p_4 in Fig.2, we can express the upper and lower edges of the broadened energy range of ω_4 with the approximation $\vartheta_r \ll 1$, respectively, [5]

$$\begin{aligned}
\overline{u}_c\langle\omega\rangle &\sim l_i u\langle\omega\rangle\gamma(1+\beta\vartheta) \equiv l_i u\langle\omega\rangle \min\{\gamma_c(1+\Delta r), \quad \gamma_r(1+\frac{1}{2}\vartheta_r^2)\} \\
\underline{u}_c\langle\omega\rangle &\sim l_i u\langle\omega\rangle\gamma(1-\beta\vartheta) \equiv l_i u\langle\omega\rangle \min\{\gamma_c(1-\Delta r), \quad \gamma_r(1-\frac{1}{2}\vartheta_r^2)\}
\end{aligned} \tag{79}$$

where l_i represents the process to choose a ω_4 within the relative line width $l_i \equiv 1 \pm \delta u_4/u$ with $\delta u_4 \equiv (\overline{u} - \underline{u})/2$ being the average value $\langle l_i\rangle = 1$, subscripts c and r in the right-hand side denote the cases where β_c and β_r are used, respectively, and $\min\{A, B\}$ requires to choose smaller one between A and B.

We then discuss the inclusive range of u by combining the broadened ω_4 in the $\langle L\rangle$-system with the intrinsic line width of the inducing laser. We introduce a notation reflecting the combining process in the $\langle L\rangle$-system

$$\omega_{<4>} \equiv l_c l_i u\langle\omega\rangle \tag{80}$$

where $l_c \equiv 1 \pm \delta u_c/u$ with $\delta u_c \equiv (\overline{u_c} - \underline{u_c})/2$ being the average value $\langle l_c\rangle = 1$, is a coefficient describing the uncertainty by the inverse transverse boost discussed above. Since the intrinsic energy uncertainties of creation and inducing laser beams are independent, the quadratic error propagation gives the following inclusive uncertainty on ω_4 in the $\langle L\rangle$-system

$$\delta^2\omega_{<4>} = \left(\frac{\partial\omega_{<4>}}{\partial l_i}\right)^2 \delta^2 l_i + \left(\frac{\partial\omega_{<4>}}{\partial l_c}\right)^2 \delta^2 l_c = u^2\langle\omega\rangle^2 \left[\left(\frac{\delta u_4}{u}\right)^2 + \left(\frac{\delta u_c}{u}\right)^2\right]. \tag{81}$$

Finally this gives the inclusive uncertainty on u

$$\delta u_{inc} \equiv \frac{\delta\omega_{<4>}}{\langle\omega\rangle} = u\sqrt{\left(\frac{\delta u_4}{u}\right)^2 + \left(\frac{\delta u_c}{u}\right)^2}, \tag{82}$$

and the upper and lower limits on u, which replace the limits in Eq.(10) with

$$\overline{u} \equiv u + \delta u_{inc} \text{ and } \quad \underline{u} \equiv u - \delta u_{inc}, \tag{83}$$

respectively, are obtained.

As a summary based on Eq.(79), the effect of the line width of the creation laser is less significant compared to that of the inducing laser for a smaller mass range, while it has some impact for a larger mass range, as long as the line width is comparable to or larger than that of the inducing laser.

[5] Note that the degree of freedom to flip p_3 and p_4 around the z-axis by keeping the angular balance in Fig.1 results in both frequency up and down shifts in ω_3 and ω_4.

Acknowledgments

K. Homma cordially thanks Y. Fujii for the long-term discussions on the theoretical aspects relevant to the scalar field in the context of cosmology. He has greatly benefited from valuable discussions with S. Sakabe, M. Hashida and Y. Nakamiya. He expresses his gratitude to T. Tajima and G. Mourou for many aspects relevant to this subject. This work was supported by the Grant-in-Aid for Scientific Research no.24654069 and 25287060 from MEXT of Japan, and also supported by MATSUO FOUNDATION.

---

[1] R. D. Peccei and H. R. Quinn, Phys. Rev. Lett. 38, 1440 (1977); S. Weinberg, Phys. Rev. Lett. 40, 223 (1978); F. Wilczek, Phys. Rev. Lett. 40, 271 (1978).

[2] Y. Fujii and K. Maeda, *The Scalar-Tensor Theory of Gravitation* Cambridge Univ. Press (2003); Mark P. Hertzberg, Max Tegmark, and Frank Wilczek, Phys. Rev. D **78**, 083507 (2008); Olivier Wantz and E. P. S. Shellard, Phys. Rev. D **82**, 123508 (2010).

[3] K. Homma, D. Habs, G. Mourou, H. Ruhl, and T. Tajima, Prog. Theor. Phys. Suppl. No. 193, (2012).

[4] T. Tajima and K. Homma, Int. J. Mod. Phys. A vol. 27, No. 25, 1230027 (2012).

[5] Y. Fujii and K. Homma, Prog. Theor. Phys. 126: 531-553 (2011), arXiv:1006.1762 [gr-qc].

[6] K. Homma, D. Habs, T. Tajima, Appl. Phys. B 106:229-240 (2012), (DOI: 10.1007/s00340-011-4567-3),arXiv:1103.1748 [hep-ph].

[7] K. Homma, Prog. Theor. Exp. Phys. 04D004 (2012).

[8] S. A. J. Druet and J.-P. E. Taran, Prog. Quant. Electr. 7, 1 (1981).

[9] Amnon Yariv, *Optical Electronics in Modern Communications* Oxford University Press (1997).

[10] F. Moulin and D. Bernard, Opt. Commun. 164, 137 (1999); E. Lundström et al., Phys. Rev. Lett. 96, 083602 (2006); J. Lundin et al., Phys. Rev. A 74, 043821 (2006); D. Bernard et al., Eur. Phys. J. D 10, 141 (2000).

[11] Y. Fujii, Nature Phys. Sci. **234**, 5 (1971); E. Fischbach and C. Talmadge. *The search for non-Newtonian gravity*, AIP Press, Springer-Verlag, New York (1998).

[12] Gerard Mourou, Bill Brocklesby, Toshiki Tajima and Jens Limpert, Nature Photonics 7, 258261 (2013).

[13] See Eq.(43.1) in J. Beringer et al. (Particle Data Group), Phys. Rev. D86, 010001 (2012).

[14] See Eq.(36.56) in J. Beringer et al. (Particle Data Group), Phys. Rev. D86, 010001 (2012).

[15] K. Ehret et al. (ALPS Collab.), Phys. Lett. B689, 149 (2010).

[16] E. G. Adelberger et al., Phys. Rev. Lett. 98, 131104 (2007); D. J. Kapner et al., Phys. Rev. Lett. 98, 021101 (2007).

[17] J. Chiaverini et al., Phys. Rev. Lett. 90, 151101 (2003).

[18] S. J. Smullin et al., Phys. Rev. D 72, 122001 (2005) [Erratum-ibid. D 72, 129901 (2005)].

[19] S. K. Lamoreaux, Phys. Rev. Lett. 78, 5 (1997) [Erratum-ibid. 81:5475 (1998)].

[20] See the parametrization, for exmple, in the section *AXIONS AND OTHER SIMILAR PARTICLES* in J. Beringer et al. (Particle Data Group), Phys. Rev. D86, 010001 (2012). And also see S. L. Cheng, C. Q. Geng, and W. T. Ni, Phys. Rev. D52, 3132 (1995) on the possible range of the ratio on the electromagnetic to color anomaly factors of the axial current associated with the axion, E/N.

[21] J. E. Kim, Phys. Rev. Lett. 43 , 103 (1979); M. A. Shifman, A. I. Vainshtein and V. I. Zakharov, Nucl. Phys. B 166 , 493 (1980).

[22] D. Bernard, arXiv:1311.5340 [physics.acc-ph].

[23] J. D. Bjorken and S. D. Drell, *Relativistic Quantum Mechanicsh*, McGraw-Hill, Inc. (1964); See also Eq.(3.80) in W. Greiner and J. Reinhardt, *Quantum Electrodynamics Second Edition*, Springer (1994).

[24] M. A. Furman, LBNL-53553, CBP Note-543.

[25] C. Möller, *General Properties of the Characteristic Matrix in the Theory of Elementary Particles. I* Munksgaard 1st edition (1946).

[26] J. F. Reintjes, *Nonlinear optical parametric processes in liquids and gases*, Academic Press, Orlando (1984).

[27] L. Novotny and B. Hecht *Principles of Nano-Optics second edition* Cambridge Univ. Press (2012); A similar description can also be found in http://www.photonics.ethz.ch/fileadmin/user_upload/optics/Courses/EM_FieldsAndWaves/AngularSpectrumRepresentation.pdf

parameters	values or comments
wavelength of creation laser λ_c	532 nm
relative line width of creation laser $(\delta\omega/\langle\omega\rangle)$	4.6×10^{-6}
wavelength of inducing laser λ_i	633 nm
relative line width of inducing laser $(\delta\omega_4/\langle\omega_4\rangle)$	3.2×10^{-6}
$u = \omega_4/\omega$ based on Eqs.(3) and (7)	0.84
focal length f	200 mm
beam diameter of laser beams d	40 mm
upper mass range given by $\vartheta < \Delta\vartheta$	0.46 eV
azimuthal asymmetric factor $\mathcal{F}_S$	$\mathcal{F}^{SC}_{1122}$ in Eq.(9)
duration time of creation laser pulse per injection τ_c	0.75 ns
duration time of inducing laser per injection τ_i (CW)	1 s
creation laser energy per τ_c	$(0.181 \pm 0.009)\mu$J
inducing laser energy per τ_i	(1.87 ± 0.19)mJ
combinatorial factor in luminosity C_{mb}	1/2
single photon detection efficiency ϵ_D	$(2.94 \pm 0.03)\%$
efficiency of the optical path 2 ϵ_{opt2}	$(4.3 \pm 0.1)\%$
branching ratio $B \equiv \epsilon_1/\epsilon_2$	0.824 ± 0.002
δN_{S2} in Eq.(22)	106

TABLE II: Experimental parameters used to obtain the upper limit on the coupling-mass relation.